ACS OMEGA

Open Access

http://pubs.acs.org/journal/acsodf

Article

Highly Efficient Photoelectrochemical Detection of Cystatin C Based on a Core−Shell MOF Nanocomposite with Biomimetic-Catalysis Amplification

Mengshi Xia,[‖] Pan Yang,[‖] Chuiyu Zhu, Yue Hu, Lichao Fang, Junsong Zheng, Xiaolong Wang,* and Yan Li*

Cite This: *ACS Omega* 2024, 9, 28228−28236

Read Online

ACCESS | Metrics & More | Article Recommendations | Supporting Information

ABSTRACT: Cystatin C (CysC) has been proven to be used to diagnose acute kidney injury (AKI) rapidly and sensitively early. Therefore, it is urgent to develop a sensitive, novel, and rapid method for detecting CysC. In this work, a novel photoelectrochemical (PEC) biosensor was designed for ultrasensitive CysC detection. Ti-MOF@DM-LZU1@Au as a photosensitive material was first modified on the ITO electrode surface. Then, Ab_1 and CysC were assembled on the electrode *via* the specific immunoresponse of an antigen and antibody. Lastly, the conjugate Ab_2/L-Cys bilayer/L-Cys-hemin/G-quadruplex with self-catalytic enzyme performance, as a signal amplification approach, could further react with CysC and Ab_1, which resulted in a stronger photocurrent. As expected, the constructed PEC sensor realized the ultrasensitive detection of CysC, with a detection range of 10 pg/mL to 16 μg/mL and a lower limit of 8.023 pg/mL. The biosensor had excellent repeatability, selectivity, and stability. Moreover, it can provide a new method for the sensitive and rapid detection of other protein molecules in clinical practice.

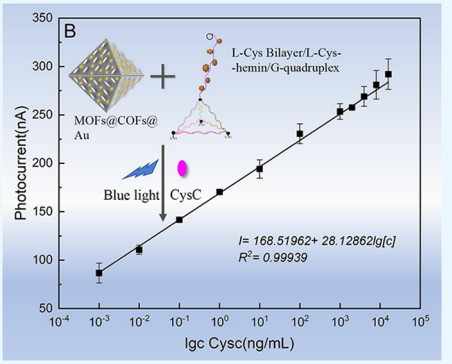

1. INTRODUCTION

Acute kidney injury (AKI) is the most common acute renal disease, whose incidence has increased over the past decade. Studies have shown that more than half of intensive care unit (ICU) patients might have AKI, and the case fatality rate is extremely high.[1] Therefore, early diagnosis and early prevention are the keys to improving the therapeutic effect of AKI. Currently, early diagnosis of AKI is based on the glomerular filtration rate (GFR) calculated from serum creatinine.[2]

Nevertheless, this detection method is inaccurate when the GFR is less than 60 mL/min.[3] Fortunately, cystatin C (CysC), an alternative filtration marker, has been proven to be used to diagnose AKI rapidly and sensitively early. Furthermore, CysC is more stable in predicting AKI than creatinine because CysC is not affected by age, sex, and lean muscle mass.[4] So far, several methods for detecting CysC have been reported, for example, immunoturbidimetry and radioimmunoassay.[5] These detection methods have high equipment costs, high labor costs, and limited sensitivity.[6] Therefore, it is extremely urgent to develop a sensitive and rapid method for detecting CysC. The photoelectrochemical (PEC) biosensor is a newly emerged electroanalytical tool.[7] Compared with traditional detection methods, PEC has the advantages of high sensitivity, fast response, low equipment cost, and convenient operation.[8] Thus, the PEC biosensor is an ideal means of detecting CysC.

The selection of photosensitive materials is the most vital consideration in the construction of the PEC sensor.[8] The metal−organic framework (MOF), a new generation of semiconductor photoelectric material, is a porous material formed by connecting metal clusters with multidentate organic linkers. Previous research has confirmed that metal clusters can be considered inorganic semiconductor quantum entities, while the organic linkers will activate the semiconductor quantum entities upon light excitation, owing to the linker-to-metal-cluster charge transfer (LCCT).[9] We chose NH_2-MIL-125 (Ti) (Ti-MOF) in this work due to its favorable characteristics, such as easy synthesis, adjustable function, high porosity, and large surface areas.[10] Especially, the Ti-MOF is more uniform in pore size compared with traditional porous materials such as mesoporous silica. The high porosity property ensures exposure of active sites on the surface of the material and promotes the production of products (electron−hole pairs). However, there are inherent problems with photoelectric materials such as Ti-MOF.

Received: February 20, 2024
Revised: June 2, 2024
Accepted: June 7, 2024
Published: June 14, 2024

Scheme 1. Schematic Illustrations of the PEC Biosensor for CysC Detection

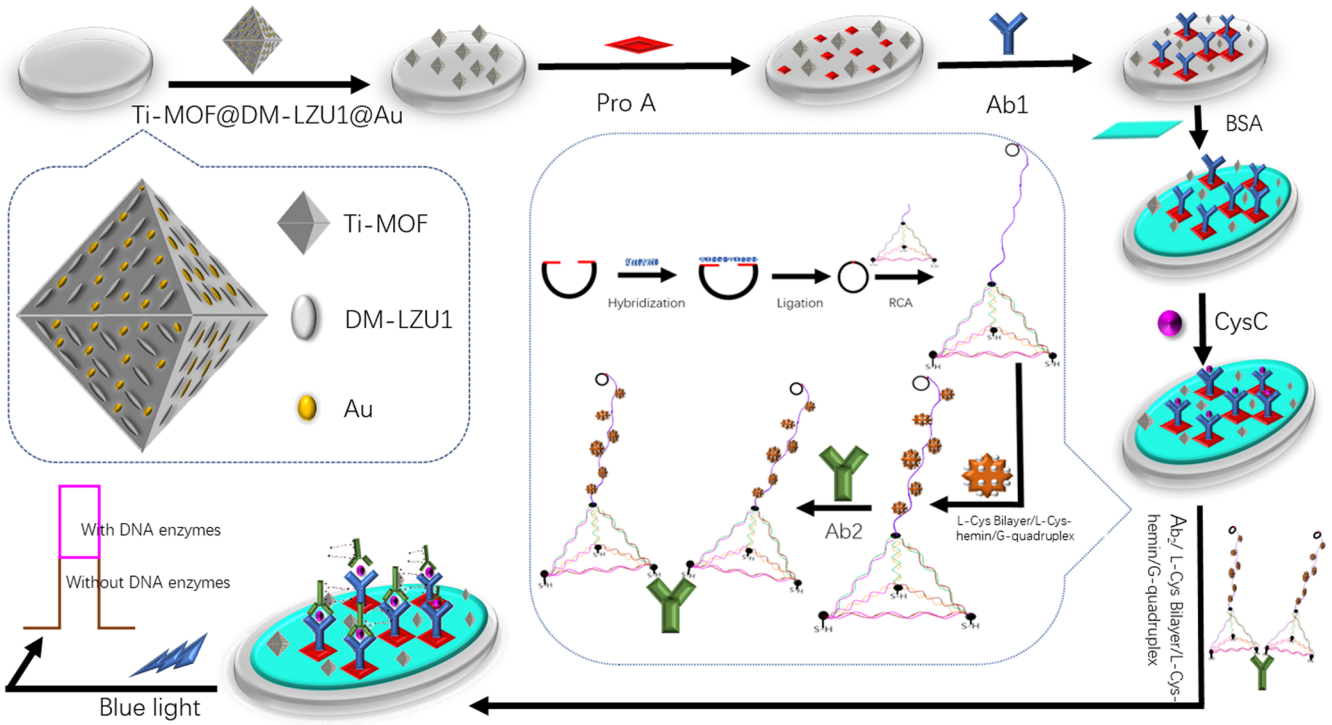

Excessive porosity of Ti-MOF can increase the charge transfer barrier to hinder charge separation; thus, the rate of photogenerated electron−hole pair recombination will aggrandize, and the photocurrent signal will diminish.[11] It is well-known that noble metals can inhibit the recombination of the photogenerated electrons and holes, for the reason that the electrons generated upon the light on the conduction band of the semiconductors can transfer to the noble metal.[12] To reduce the electron−hole recombination rate and maximize Ti-MOF's performance for photochemical detection, gold nanoparticles (AuNPs), which have the advantages of good biocompatibility and easy surface modification, are loaded inside the pores of Ti-MOF. Regretfully, the size of the nanopores of the Ti-MOF is so tiny that the loaded AuNPs may block some of the pores, thus resulting in an electron−hole separation barrier.[13]

The literature has reported that the covalent organic framework (COF) can solve the above problems. The COF is a network porous polymer synthesized from light elements such as C, H, O, and N.[14] In this experiment, COF-LZU1 (DM-LZU1) is gathered on the surface of the Ti-MOF, and AuNPs are limited to the interface pores built between Ti-MOFs and DM-LZU1, so as not to block some pores of the Ti-MOFs. Therefore, the obtained Ti-MOF@DM-LZU1@Au shows an excellent photocurrent signal under light irradiation.[15]

Simultaneously, in this work, the L-cysteine (L-Cys) bilayer/L-Cys-hemin/G-quadruplex was applied for the first time in a PEC sensor as a self-catalytic enzyme with efficient autocatalysis. The traditional strategy of hemin/G-quadruplex achieves signal amplification by converting Fe(III)/Fe(II) of hemin in the H_2O_2 solution; hemin/G-quadruplex can accept electrons from photosensitive materials to reduce the recombination rate of electron−hole pairs.[16] However, the above strategy has fatal drawbacks. H_2O_2 will suffer instability and decomposition when the traditional hemin/G-quadruplex reacts.[17] Su et al. have found that L-Cys can be regarded as a stable catalytic substance to construct the L-Cys/hemin/G-quadruplex self-catalytic platform, which simultaneously mimics the biocatalytic functions for the H_2O_2 reduction and L-Cys oxidation.[18] This strategy can generate H_2O_2 in situ, where a fixed amount of H_2O_2 is formed by a more stable substrate (L-Cys).

The occurrence of the catalytic reaction depends on the binding of L-Cys to the active center of the hemin/G-quadruplex.[19] However, in the structure of L-cys/hemin/G-quadruplex, L-Cys spreads to the active center of hemin/G-quadruplex only by Brownian motion,[20] so the catalytic efficiency is limited by the relatively low binding affinity between hemin/G-quadruplex and L-Cys. However, the research team led by Li[19] confirms that the L-Cys-hemin/G-quadruplex possesses a better affinity to L-Cys compared with that of the hemin/G-quadruplex. Based on the above research, we combined hemin/G-quadruplex and L-Cys into one molecule to form L-Cys-hemin/G-quadruplex; then, a large amount of L-Cys can be enriched around the surface of L-Cys-hemin/G-quadruplex to form L-Cys bilayer/L-Cys-hemin/G-quadruplex *via* hydrogen-bond and electrostatic interaction. In this way, L-Cys and the active center of hemin/G-quadruplex can be closely combined, which is beneficial to catalytic enhancement. In addition, in this work, G-quadruplex is formed by the RCA reaction,[16] triggered by the single-stranded DNA primer extended from the vertex of the DNA tetrahedron. We can thus obtain countless amplifiers with efficient autocatalytic functions that achieve significant amplification of photocurrent signals for sensitive detection.

Herein, a novel PEC sensor, based on Ti-MOF@DM-LZU1@Au as a photosensitive material and the L-Cys bilayer/L-Cys-hemin/G-quadruplex as a self-catalytic enzyme, was designed for ultrasensitive CysC detection (Scheme 1). Ti-

https://doi.org/10.1021/acsomega.4c01644
ACS Omega 2024, 9, 28228−28236

MOF@DM-LZU1@Au was first modified on an indium tin oxide (ITO) electrode as a substrate material. Then, the protein A (proA) was added to the ITO/Ti-MOF@DM-LZU1@Au electrode to immobilize and orient the Ab_1 to form ITO/Ti-MOF@DM-LZU1@Au/proA/Ab_1.[21] Next, the target protein CysC was captured by the electrode *via* the specific immunoresponse of the antigen and antibody. The photocurrent signal gradually weakened with more additives on the electrode surface. However, the conjugate Ab_2/L-Cys bilayer/L-Cys-hemin/G-quadruplex, as a signal amplification approach, could further react with CysC and Ab_1, which resulted in a stronger photocurrent. Therefore, a sandwich-type photoelectrochemical immunosensor with the assistance of signal amplification was constructed that could detect CysC sensitively. This proposed self-catalytic enzyme offers a novel approach for the detection of immunoreactions and provides new insights into the diagnosis of other protein biomarkers.

2. EXPERIMENTAL SECTION

2.1. Materials and Reagents. All DNA sequences in this study (Table S1 in the Supporting Information), T_4 DNA ligase, Bst DNA polymerase, and the corresponding buffer were purchased from Shanghai Sangon Biotechnology Co. (China). The deoxynucleotide solution mixture (dNTPs) was purchased from Solarbio Co. (China). 1,3,5-Triformylbenzene (TFB), 2-aminoterephthalate (H_2ATA), cetrimonium bromide (CTAB), bovine serum albumin (BSA), and *p*-phenylenediamine (PDA) were obtained from Aladdin (China). Anhydrous *N*,*N*-dimethylformamide (DMF), 1-(3-dimethylaminopropyl)-3-ethylcarbodiimide (EDC), *N*-hydroxy succinimide (NHS), and 1,4-dioxane were purchased from Macklin Co. (China). Chloroauric acid ($HAuCl_4$), tris(2-carboxyethyl) phosphine (TCEP), and L-ascorbic acid (AA) were purchased from Sigma-Aldrich Co. (USA). CysC, Ab_1, and Ab_2 were purchased from Chengdu Zen-Bioscience Co. (China). Tris(hydroxymethyl) aminomethane (THAM) and dimethyl sulfoxide (DMSO) were purchased from MedChemExpress Co.

2.2. Apparatuses. The photocurrent response was measured on a PEC apparatus (IVIUM, IM2501, Netherlands). The ITO electrodes were cleaned in an ultrasonic cleaning apparatus (HECHUANG, KH-300DE, China). The characterization of Ti-MOF@DM-LZU1@Au was carried out by scanning electron microscopy (SEM, S4800 Hitachi, Japan) and transmission electron microscopy (TEM Philips, TECNAI10, Netherlands).

2.3. Experiment Principle. As is shown in Scheme 1, the experiment was roughly divided into three parts: (1) the synthesis of the composite material Ti-MOF@DM-LZU1@Au, (2) construction of L-Cys bilayer/L-Cys-hemin/G-quadruplex, and (3) composition of the photoelectrochemical immunosensor. In the first step, Ti-MOF@DM-LZU1@Au, as a photosensitive material, was synthesized by the thermal synthesis method and redox method. When Ti-MOF@DM-LZU1@Au was illuminated by blue light, electron−hole pairs were generated by electrons that move from the valence band to the conduction band. Compared with single-molecule materials, composite materials could better inhibit the recombination of electron−hole pairs, enhancing the photocurrent. We constructed the DNA tetrahedron and the circular DNA template in the second step. Then, the single-stranded primer, derived from the top of the DNA tetrahedron, was tightly combined with a circular DNA template to initiate an RCA reaction to produce a repeat sequence of the circular probe, which can form a G-quadruplex later. Meanwhile, L-Cys bilayer/L-Cys-hemin, as the target signal amplifier, was synthesized. Furthermore, we also prepared two other signal amplifiers, hemin and L-cys-hemin, to compare with our target signal amplifier. Finally, the target signal amplifier was implanted into G-quadruplex to gain the L-Cys bilayer/L-Cys-hemin/G-quadruplex structure as DNases with efficient autocatalytic functions. In the experiment, Ti-MOF@DM-LZU1@Au was modified on the ITO electrode to fabricate the immunosensor. Subsequently, capture antibodies (Ab_1) were anchored to the electrode using proA as the linking molecules. After blocking of unbound sites with BSA,[22] the immunosensor was incubated with varying concentrations of CysC and then immobilized with an Ab_2/L-Cys bilayer/L-Cys-hemin/G-quadruplex conjugate signal amplification tag. Lastly, the sensor system in a solution of H_2O_2 would generate a current signal. However, only a weak current signal was produced without the CysC. Therefore, we could detect the concentration of CysC through the relationship between photocurrent changes and CysC. The designed PEC sandwich immunoassay gave an excellent performance with high sensitivity, selectivity, and good accuracy using actual samples.

2.4. Construction of DNA Tetrahedra. DNA tetrahedra were synthesized by one-step thermal denaturation according to a previous report.[23] The equal volume and equimolar ratio of DNA single strands S_1, S_2, S_3, and S_4 were mixed for 5 min, and then, the mixture was put into a TM buffer (10 mM Tris and 5 mM $MgCl_2$). Finally, the final products were incubated for 10 min at 95 °C by a PCR instrument and cooled to 4 °C for 30 s immediately.

2.5. RCA System. *2.5.1. Preparation of the Circular Template.* The first step was to hybridize the linear padlock probe (10 μM) with the DNA T_1 (10 μM); the volume of both was 5 μL; then, we incubated the mixture for 3 min at 95 °C and then cooled it to room temperature. In the second step, 2 μL of the T_4 DNA ligase, 2 μL of the T_4 DNA ligase buffer, and 6 μL of DI water were added to the above mixture to obtain the intermediate product, which would be stored at 22 °C for 12 h, and the enzyme reaction was terminated at 65 °C for 10 min. In the last step, 1 μL of Bst DNA polymerase and 2 μL of the associated buffer were added to the intermediate product; then, they were mixed and incubated at 22 °C for 24 h. Finally, the enzyme was inactivated at 75 °C for 10 min.

2.5.2. RCA Reaction. The RCA reaction was performed in 20 μL of a buffer containing 2 μL of the Bst DNA polymerase buffer, 5 μL of the DNA tetrahedron, 2 μL of the circular template, 2 μL of dNTPs, 7 μL of DI water, and 2 μL of the Bst DNA polymerase. The whole process lasted for 2 h at 37 °C and was terminated by incubation at 95 °C for 10 min.

2.6. Formation of the G-quadruplex. The product produced by the RCA reaction was put into the solution containing THAM (200 mM), KCl (40 mM), NaCl (400 mM), Triton-100% (0.1%), and DMSO (1%) to form the G-quadruplex.

2.7. Building the Ab_2/L-Cys Bilayer/L-Cys-Hemin/G-quadruplex. *2.7.1. Construction of the L-Cys Bilayer/L-Cys-Hemin/G-quadruplex.* Hemin (20 μL, 5 mM) reacted with EDC/NHS (2 μL each) to activate the carboxyl of hemin. To obtain the L-Cys-hemin, L-Cys (0.3 M) was added to the above mixture solution and stirred for 12 h at 4 °C. Then, 5 μL of L-Cys-hemin solution and 20 μL of the G-quadruplex synthesized and mentioned above were mixed and stirred for

https://doi.org/10.1021/acsomega.4c01644
ACS Omega 2024, 9, 28228−28236

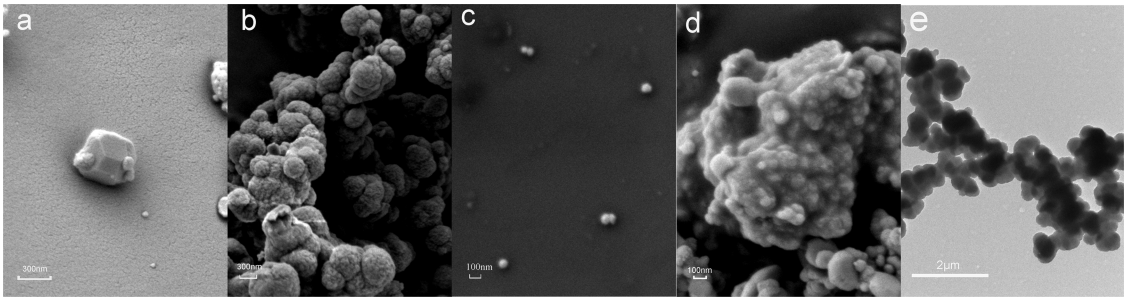

Figure 1. SEM images of (a) Ti-MOF, (b) DM-LZU1, (c) AuNPs, and (d) Ti-MOF@DM-LZU1@Au. (e) TEM image of Ti-MOF@DM-LZU1@Au.

2 h at 24 °C to form the L-Cys-hemin/G-quadruplex. Lastly, to form L-Cys bilayers, L-Cys-hemin/G-quadruplex was dispersed in an L-Cys (10 mM) solution containing TCEP (10 mM), which was used to avoid L-Cys being oxidized.

2.7.2. Preparation of Au Nanoparticle Colloids. $HAuCl_4$ (0.01% W/V) was added to 100 mL of DI water in a conical flask. After the solution has been heated sufficiently, 4 mL of trisodium citrate (1% W/V) was added to the conical flask with quick-stirring liquid subsequently to form a wine red solution. Ultimately, Au nanoparticle colloids were obtained.

2.7.3. Construction of Ab_2/L-Cys Bilayer/L-Cys-Hemin/G-quadruplex. First, the pH of Au nanoparticle colloids was adjusted to 9.0 with Na_2CO_3. Second, 200 μL of Ab_2 (0.5 mg/mL) was injected into 4 mL of alkalized Au nanoparticle colloids; then, they were shaken gently, and the reaction lasted for 2 h. Finally, the L-Cys bilayer/L-Cys-hemin/G-quadruplex was added to the above solution, and the reaction was kept for another 2 h at 4 °C to build the Ab_2/L-Cys bilayer/hemin/G-quadruplex.

2.8. Synthesis of Ti-MOF@DM-LZU1. *2.8.1. Synthesis of Ti-MOF.* Ti-MOF was synthesized by following the previously reported procedures.[24] A 0.543 g amount of H_2ATA and 0.26 mL of $Ti\{OCH(CH_3)_2\}_4$ (0.87 mM) were mixed with the solution containing anhydrous DMF and anhydrous MeOH. The resulting mixed solution was stirred at room temperature for 5 min and then transferred to a 50 mL Teflon liner and heated at 150 °C. After 3 days, the obtained suspension was centrifuged, washed with DMF and MeOH, and dried under vacuum to get the yellow solid product, Ti-MOF.

2.8.2. Synthesis of DM-LZU1. TFB (64 mg, 0.3 mmol), 64 mg of PDA (0.3 mmol), and 4 mL of 1,4-dioxane were mixed and stirred for 10 min to obtain a clear solution. Next, 0.8 mL of acetic acid (3 M) was added dropwise to the clear solution, forming a yellow precipitate. After 3 days of reaction at room temperature, the above precipitate was centrifuged and washed with tetrahydrofuran, acetone, and methanol; in turn, the bright yellow powder called DM-LZU1 was formed by vacuum drying.

2.8.3. Synthesis of Ti-MOF@DM-LZU1. A 60 mg portion of Ti-MOF was added into the 1,4-dioxane solution containing TFB. Then, the mixture solution was sonicated for 20 min. Subsequently, 0.4 mL of acetic acid was dropwise added to the solution and continued to sonicate for another 20 min. Next, 2 mL of the 1,4-dioxane solution containing 16 mg of PDA was dropped into the above solution and gently stirred for 1 h. After 3 days of reaction at room temperature, the above solution was centrifuged and washed with tetrahydrofuran, acetone, and methanol in turn and dried under vacuum to get Ti-MOF@DM-LZU1.

2.9. Preparation of AuNPs. *2.9.1. Preparation of the Au Seed.* The systematic procedure followed the literature with minor modifications.[25] First, 100 μL of $HAuCl_4$ (24.28 mM) was mixed with 7.5 mL of CTAB (0.1 M) solution; then, 1.8 mL of DI water was added to the mixture. Second, 0.6 mL of cold $NaBH_4$ (0.01 M) was added to the above solution under the condition of quick stirring to obtain a Au seed suspension. Simultaneously, the solution became light brown from luminous yellow. The solution was left undisturbed for 3 h at room temperature.

2.9.2. Preparation of Growth Solution. The growth solution was composed of CTAB (100 mL, 0.1 M), $HAuCl_4$ (2 mL, 24.28 mM), H_2SO_4 (2 mL, 0.5 M), $AgNO_3$ (1 mL, 10 mM), and AA (0.8 mL, 0.1 M).

2.9.3. Preparation of AuNPs. The Au seed (0.24 mL) was added to the growth solution, the mixture solution slowly became red after 30 min, and the whole reaction was almost complete. The AuNP suspension was centrifuged at 12,000 rpm for 5 min to obtain the sediment; later, it was resuspended in 10 mL of DI water.

2.10. Construction of Ti-MOF@DM-LZU1@Au. The suspensions of Ti-MOF@DM-LZU1 and AuNPs were mixed at a 1:1 volume ratio, and then, the mixture was stirred at high speed for 5 min and left undisturbed for 24 h to obtain composite particles, Ti-MOF@DM-LZU1@Au.

2.11. Fabrication of the Photoelectric Chemical Immunosensor. The ITO electrodes were first cleaned by ultrasonic treatment for 10 min in acetone, ethanol, and ultrapure water in sequence and then dried at 90 °C. The 10 μL Ti-MOF@DM-LZU1@Au mixture with chitosan was coated on the cleaned ITO electrode and allowed for drying naturally. Then, 10 μL of proA was dripped onto the electrode surface and dried at 24 °C for 40 min to immobilize and orient Ab_1.[26] Next, 10 μL of Ab_1 was added dropwise to the surface of ITO/Ti-MOF@DM-LZU1/proA and kept at 24 °C for 1 h. To wash off excess Ab_1 molecules, the ITO/Ti-MOF@DM-LZU1@Au/proA/Ab_1 electrode was incubated with 1 wt % BSA for 1 h for blocking the nonspecific binding sites at 24 °C. To capture the CysC antigen, the ITO/Ti-MOF@DM-LZU1@Au/proA/Ab_1/BSA electrode was incubated with 10 μL of the antigen for 1 h at 4 °C. Lastly, 10 μL of the Ab_2/L-Cys bilayer/L-Cys-hemin/G-quadruplex as a signal amplifier was added to the electrode for 24 h at 4 °C to form a sandwich immunosensor. After each reaction was completed, the electrodes were rinsed with DI water and dried. Finally, the prepared PEC immunosensor was detected in PBS solution containing 12 mM H_2O_2, which acted as sacrificial reagents offering electrons to the PEC electrode. Lastly, the blue laser with a spectral range of 400−480 nm was used as an irradiation

https://doi.org/10.1021/acsomega.4c01644
ACS Omega 2024, 9, 28228−28236

source, and it was switched on and off every 10 s. The electrochemical method was chronoamperometry, and the external voltage was 0.0 V.

3. RESULTS AND DISCUSSION

3.1. Characterization of Ti-MOF@DM-LZU1@Au. To investigate the crystal structure of the composite material Ti-MOF@DM-LZU1@Au, we used X-ray powder (XRD) patterns to characterize it, as shown in Figure S1. The X-ray diffraction peak of Ti-MOF (curve a) was mainly concentrated in the range of 6−12, 14−20, and 31−33°.[27] On the contrary, the diffraction peak intensity of DM-LZU1 (curve b) was very weak, so we found that there was no significant difference in the XRD patterns of Ti-MOF@DM-LZU1 (curve c) and Ti-MOF (curve a). After being compounded with AuNPs, distinctive diffraction peaks belonging to AuNPs appeared at 38.095 and 44.391°.

Figure 1a−d shows the SEM morphologies of Ti-MOF, DM-LZU1, AuNPs, and Ti-MOF@DM-LZU@Au composite nanoparticles at different test multiples. Judging from the pictures, we could see that Ti-MOF was smooth octahedrons, DM-LZU1 had a compact lamellar morphology, AuNPs were shaped like millet grains, and AuNPs were evenly distributed on the surface of Ti-MOF@DM-LZU.

In the meantime, TEM also investigated the morphology of the Ti-MOF@DM-LZU. The TEM image (Figure 1e) of the Ti-MOF@DM-LZU revealed that in contrast to the smooth surface of pristine Ti-MOF, the surface of Ti-MOF in the Ti-MOF@DM-LZU hybrid was well-covered by the vertically grown DM-LZU nanosheets. All the above results demonstrated the successful recombination of the three particles from the perspective of morphology.

In order to further demonstrate the successful synthesis of the composite material, Ti-MOF, Ti-MOF@DM-LZU1, and Ti-MOF@DM-LZU1@Au were studied by FT-IR analysis to investigate the interaction between them further. As is demonstrated in Figure S2, the FT-IR spectrum of the Ti-MOF (curve a) showed the typical stretching band for the −C═N at ≈1619 cm^{-1} indicating the formation of imine-linked bonds. However, the spectra of DM-LZU1 (curve b) and Ti-MOF@DM-LZU1 (curve c) had no obvious absorption peak. However, when we compared and analyzed the infrared spectra of Ti-MOF@DM-LZU1@Au (curve d) and Ti-MOF@DM-LZU1, we found that Ti-MOF@DM-LZU1@Au had an obvious new absorption peak at 1154.52 cm^{-1}; this was attributed to the vibration absorption of the C−N bond from CTAB molecules coated on the surface of AuNPs. It demonstrated that there was no new chemical bond generated during the composite process of Ti-MOF@DM-LZU1 and AuNPs, and the bonding process was a physical change. In summary, we have confirmed the successful synthesis of Ti-MOF@DM-LZU1@Au from a microscopic point of view.

3.2. Characterization of the DNA Tetrahedron and RCA Products. The DNA tetrahedron was characterized by 6% polyacrylamide gel electrophoresis (PAGE) at 120 V for 40 min.[28] The results are represented in Figure 2 below. From left to right in Figure 2, the six lanes were the Marker band, single-stranded S_1, S_2, S_3, and S_4, and the synthesized DNA tetrahedron. Small DNA molecules moved faster than larger molecules because the larger molecules suffered more excellent resistance when passing through the pores of the agarose gel.

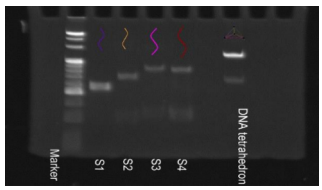

Figure 2. Polyacrylamide gel electrophoresis characterization of the DNA tetrahedron.

The results confirmed that the DNA tetrahedron was successfully assembled.

In Figure 3, agarose gel electrophoresis, real-time fluorescence, and TEM were used to evaluate the formation of RCA products. Agarose gel electrophoresis (1 %) was performed at 110 V to verify the success of RCA progress (Figure 3a). The four lanes were the Marker band, DNA tetrahedron, single-stranded S_3, and the products synthesized by RCA. Obviously, the fourth lane moved the slowest, and the results indirectly indicated the success of the RCA process. In addition, we could find long DNA products amplified by RCA from the TEM image (Figure 3b). Finally, when the linear padlock probe hybridized with DNA single-strand T_1 to form a loop, both ends of the linear padlock probe were complementary to the ends of T_1 to form a DNA double strand. The SYBR fluorescent dye can be incorporated into the DNA double strand. Therefore, with the progress of RCA, the number of DNA double strands multiplied, and the fluorescent signal also increased, as shown by curve A in Figure 3c. On the contrary, when the looping process failed, there was no fluorescence effect, like curve B in Figure 3c.

3.3. Characterization and Identification of Electrochemical Biosensor Construction. Figure 4A exhibits the characterization of the assembly process of the biosensor by the electrochemical impedance spectrum (EIS). The entire detection process was measured in 5 mM $K_3Fe(CN)_6$ and $K_4Fe(CN)_6$ solutions containing 0.1 M KCl. The R_{et} of the bare ITO electrode (curve a) was about 18 Ω. When Ti-MOF@DM-LZU1@Au was fixed on the surface of the ITO electrode, the R_{et} increased to about 90 Ω (curve b). After the vertical deposition of proA was added to the electrode surface, an obviously decreased R_{et} was observed (curve c, R_{et} ≈ 845 Ω). When Ab_1 and CysC were continuously immobilized on ITO/Ti-MOF@DM-LZU1@Au/proA, R_{et} was about 1006 (curve d) and 1148 Ω (curve e). Furthermore, after Ab_2/L-Cys bilayer/L-Cys-hemin/G-quadruplex was fixed on the surface of the electrode, the R_{et} was increased to1388 Ω (curve f) due to the retardation of electron transfer *via* the increased steric hindrance effect.

Cyclic voltammetry (CV), a helpful technology for the characterization of electrode modification, was performed step by step in 2 mM $K_3Fe(CN)_6$ and $K_4Fe(CN)_6$ containing 0.1 M KCl with a potential range from −0.3 to 0.7 V at a scan rate of 50 mV/s (Figure 4B). The bare ITO electrode exhibited a pair of well-defined redox peaks of $[Fe(CN)_6]^{3-/4-}$ (curve a). When Ti-MOF@DM-LZU1@Au was fixed on the ITO electrode, an apparently increased peak current with a decreased oxidation−reduction potential (curve b) was obtained, which was due to the good electrical conductivity of the Ti-MOF@DM-LZU1@Au. After proA (curve c) and Ab_1 (curve d) were immobilized onto the surface of the electrode, the peak current was reduced obviously, and the oxidation−reduction potential was increased obviously. When

https://doi.org/10.1021/acsomega.4c01644
ACS Omega 2024, 9, 28228−28236

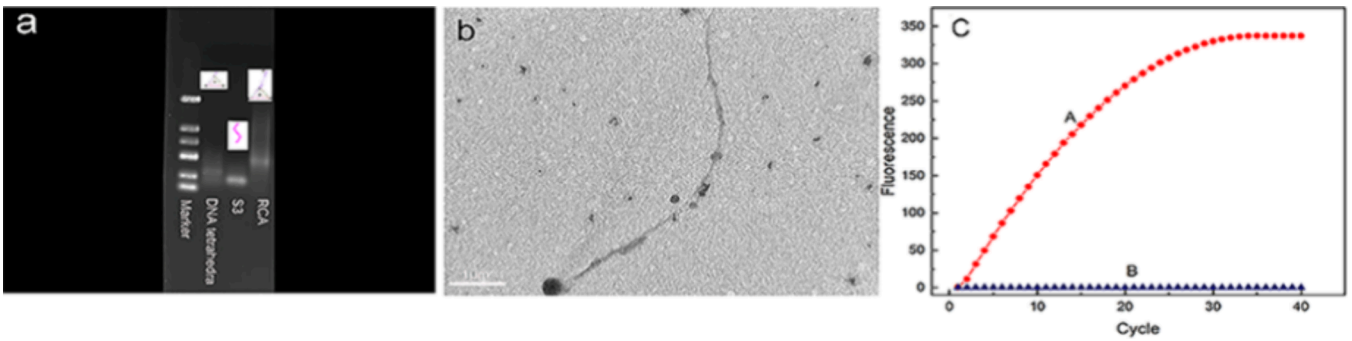

Figure 3. (a) Agarose gel electrophoresis characterization of the products of the RCA reaction. (b) TEM image of the products of the RCA reaction. (c) Real-time fluorescence monitoring of the RCA reaction.

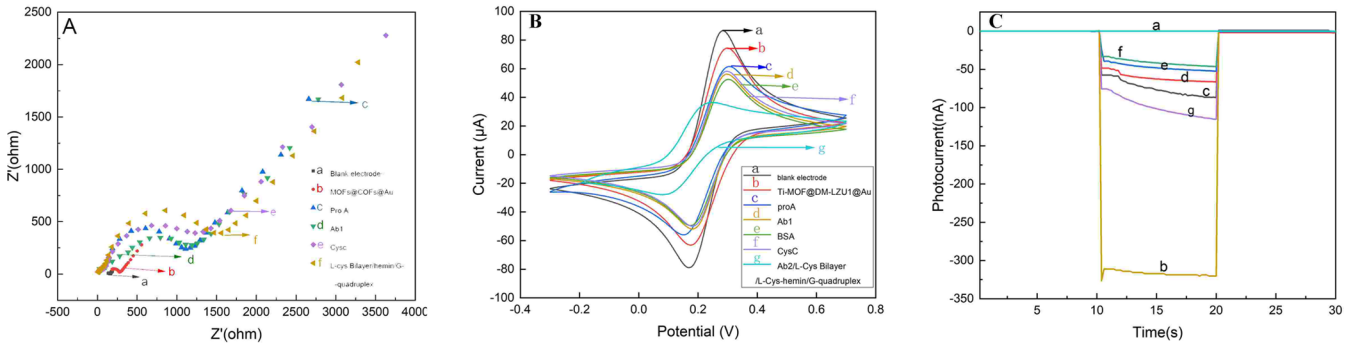

Figure 4. (A) Characterizations for constructing the PEC biosensor based on electrochemical impedance spectroscopy: (a) blank electrode, (b) Ti-MOF@DM-LZU1@Au, (c) ProA, (d) Ab_1, (e) CysC, and (f) Ab_2/L-Cys bilayer/L-Cys-hemin/G-quadruplex; (B) cyclic voltammetry: (a) ITO, (b) Ti-MOF@DM-LZU1@Au, (c) ProA, (d) Ab_1, (e) BSA, (f) CysC, and (g) Ab_2/L-Cys bilayer/L-Cys-hemin/G-quadruplex; (C) PEC responses of (a) ITO, (b) Ti-MOF@DM-LZU1@Au, (c) ProA, (d) Ab1, (e) BSA, (f) CysC, and (g) Ab_2/L-Cys bilayer/hemin/G-quadruplex.

BSA was used to block nonadsorbed sites on the electrode surface (curve e), the peak current was decreased obviously, which was mainly due to the inhibition of BSA for electron transfer. Then, with the reaction with CysC, the peak current was further reduced (curve f). This could be mainly due to the insulation of CysC. In the end, the biosensor reacted with Ab_2/L-Cys bilayer/L-Cys-hemin/G-quadruplex. Because the steric hindrance effect increased, we found that the peak current dramatically decreased (curve g). The measured results of CV and EIS were consistent. Both of these indicate that the photoelectrochemical biosensor was successfully constructed.

3.4. PEC Characterization of Biosensors. The photogenerated electron transfer process of the biosensor was performed in the H_2O_2 electrolyte solution (Figure 4C). There was no obvious photocurrent response for the bare ITO electrode (curve a). After the modification of Ti-MOF@DM-LZU1@Au on the electrode surface, a high photocurrent signal was produced under blue light (curve b). Then, proA (curve c), Ab_1 (curve d), BSA (curve e), and CysC (curve f) were successively modified on the surface of the electrode; due to the weakening of electron transfer capacity, protein steric hindrance, and other factors, the photoelectric signal was greatly reduced. In the end, Ab_2/L-Cys bilayer/L-Cys-hemin/G-quadruplex was fixed to the processed sensor through an immunoreaction (curve g). The photocurrent signal would be higher than before due to the reduction of steric hindrance caused by the L-Cys bilayer.

3.5. Optimization of Sensor Conditions. To obtain the best photosensitive material, we prepared four kinds of materials; they were Ti-MOF, DM-LZU1, Ti-MOF@DM-LZU1, and Ti-MOF@DM-LZU1@Au (Figure S3A). The photocurrent brought by Ti-MOF@DM-LZU1@Au was the strongest, which was mainly due to its advantages of high porosity, low electron−hole recombination rate, and large surface area. Therefore, we chose it as the photosensitive material.

Because the AuNPs could inhibit the recombination of the photogenerated electrons and holes, a suitable ratio of Ti-MOF@DM-LZU1 and AuNPs had a great influence on the photoelectric properties. We prepared 5 different mass ratios of Ti-MOF@DM-LZU1 and AuNP solutions (0.25:1, 0.5:1, 0.75:1, 1:1, and 1:1.25) to confirm the most suitable ratio of Ti-MOF@DM-LZU1 and AuNPs. Figure S3B shows that the photocurrent reached the strongest when the ratio of Ti-MOF@DM-LZU1 and AuNPs was 1:1. However, once the ratio was greater than 1:1, the signal showed a downward trend because the loaded AuNPs might block some pores of Ti-MOF@DM-LZU1, thus resulting in an electron−hole separation barrier.

H_2O_2, as the electron donor, played the role of electron transfer in the detection system. To confirm the best concentration of H_2O_2 electrolyte solution, different concentrations of H_2O_2 (4, 8, 12, 16, and 20 mM) were prepared. As is shown in Figure S3C, the photocurrent reached the maximum at 12 mM; then, the photocurrent trend flattened out, which might be due to saturation of electron transfer.

ProA could fix Ab_1 on the electrode surface in an orderly manner to improve the performance of the sensor. It could be seen from Figure S3D that in the range of 0.025−0.2 mg/mL, when the concentration of proA reached 0.1 mg/mL, the sensor showed the strongest photocurrent.

https://doi.org/10.1021/acsomega.4c01644
ACS Omega 2024, 9, 28228−28236

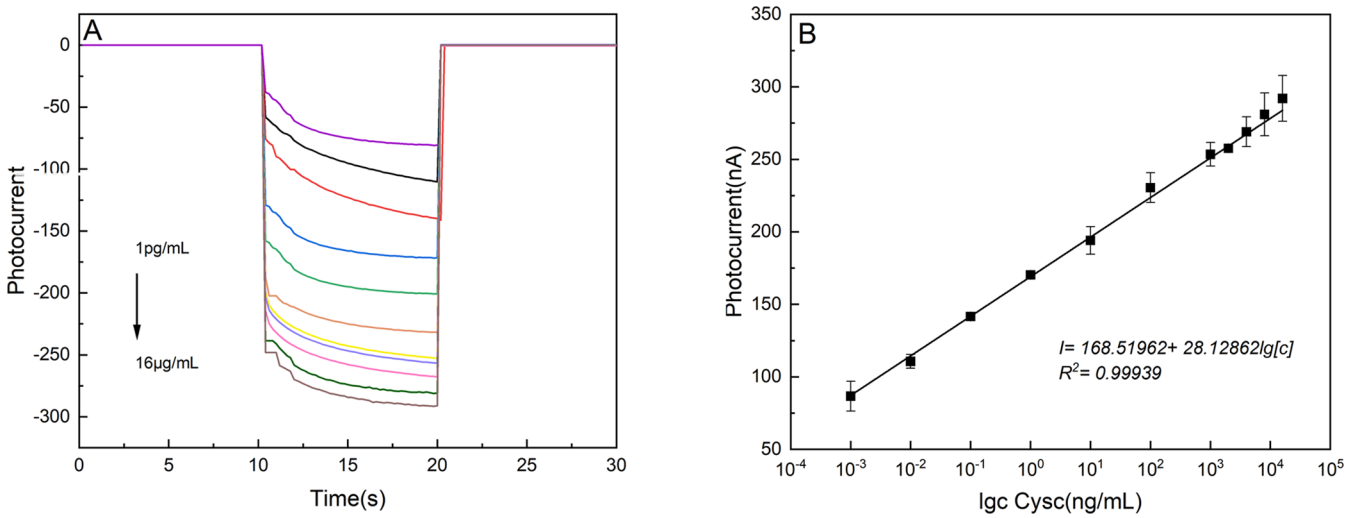

Figure 5. PEC response (A) and linear calibration curve (B) of the biosensor with different concentrations of CysC, from 1 pg/mL to 16 μg/mL.

3.6. Comparison of Different Signal Amplification Strategies. Three different signal amplification strategies were prepared in our experiment: (1) Only hemin was present, forming a hemin/G-quadruplex (curve a). (2) L-Cys combined with hemin to form the L-cys/hemin/G-quadruplex (curve b). (3) Bilayer L-cys and L-cys-hemin formed L-cys bilayers/L-cys-hemin/G-quadruplex (curve c). Figure S4 shows that the photocurrent brought by L-cys bilayers/L-cys-hemin/G-quadruplex was the strongest; this could be owing to the stability advantage of L-Cys bilayers/L-cys-hemin/G-quadruplex. In addition, the L-cys bonded closely to the active center of hemin/G-quadruplex in L-cys bilayers/L-cys-hemin/G-quadruplex, which enhanced the catalytic activity by the self-catalytic thiol oxidation of L-Cys-hemin/G-quadruplex, as well as the fast redox reaction of L-cys with the assistance of L-cys double layers and TCEP. It further proved that the signal amplification strategy in this experiment was feasible.

3.7. PEC Performance with CysC. The PEC biosensor was prepared according to the optimal conditions obtained in the experiment and then using different concentrations of CysC (10^{-3}, 10^{-2}, 0.1, 1, 10, 10^2, 10^3, 2×10^3, 4×10^3, 8×10^3, and 16×10^3 ng/mL) for photocurrent response detection (Figure 5A). As the concentration of CysC increased, more Ab_2/L-Cys bilayers/L-Cys-hemin/G-quadruplex was bound with CysC by the immunoresponse, and a stronger photocurrent response can be generated. With the wide range of concentrations from 1 pg/mL to 16 μg/mL, the photocurrent signal increased linearly with the increase of the logarithm of target CysC. (Figure 5B shows a linear regression equation $I = 168.51962 + 28.12862 \lg[c]$ ($R^2 = 0.99939$) in the concentration range from 1 pg/mL to 16 μg/mL, with a detection limit (LOD) of 8.023 pg/mL. The obtained CysC detection range and LOD were better than the previous methods reported in the literature (Table 1). It proved that the sensor that we designed had good sensitivity and a wider linear range.

3.8. PEC Biosensor Performance Detection. The specificity was investigated by measuring the photocurrent of the prepared electrodes using five different types of proteins.[29] As is shown in Figure S5A, the sensor was respectively incubated in PSA (1000 ng/mL), HCG (1000 ng/mL), and CysC (1000 ng/mL) solutions; CysC had a much stronger photocurrent response than others. In addition, the photocurrent responses of prostate specific antigen (PSA), chorionic gonadotropin (HCG), and the blank protein were almost the same. The mixture protein solution of CysC containing HCG and PSA had no apparent change in the photocurrent compared to CysC. The above results could be primarily attributed to the specific recognition of the CysC antigen and antibody. It also indicated that the prepared PEC sensor had good specificity for CysC determination.

Table 1. Comparison with Previous Detection Methods on CysC

detection strategy	linear range	limit of detection	refs
PEC	0.72 pM−3.6 nM	0.14 pM	30
electrochemical capacitor	0.3 μg/mL	0.028 μg/mL	31
electrochemical immunosensor based on SPE	0.01−0.1 μg/mL	66 ng/mL	32
PEC	0.72 pM−7.19 nM	0.16 pM	33
PEC	10^{-6}−16 μg/mL	8.023 pg/mL	this work

The repeatability was assessed by measuring the photocurrent of five independently prepared electrodes, which were treated with 1 μg/mL CysC. As shown in Figure S5B, the relative standard deviation (RSD) was 3.25%, suggesting that the sensor had good repeatability.

To evaluate the stability of the PEC sensor, the assembled sensor was stored in a refrigerator at 4 °C and tested once a week. After 4 weeks, the photocurrent maintained 92% of the initial signal, which showed excellent stability (Figure S5C).

3.9. Practical Application of the PEC Sensing System. To evaluate the application of the proposed PEC biosensor in clinical diagnosis, it was employed for the detection of CysC in human serum samples. As shown in Table 2, the recovery rate of CysC was 87.5−106%, which showed that the PEC sensor system proposed in this experiment had good clinical application value.

4. CONCLUSIONS

To summarize, in this experiment, we successfully synthesized the photosensitive material Ti-MOF@DM-LZU1@Au, which

https://doi.org/10.1021/acsomega.4c01644
ACS Omega 2024, 9, 28228−28236

Table 2. Analysis Results of CysC Recovery in the Human Serum by the PEC Sensor

sample	added (ng/mL)	found (ng/mL)	recovery (%)
1	0.001	0.00102	102
2	0.01	0.0095	95
3	0.1	0.0938	93.8
4	1	1.0052	100.52
5	10	9.85	98.5
6	100	87.5	87.5
7	10^3	1.01×10^3	101.4
8	2×10^3	2.1×10^3	106
9	4×10^3	3.88×10^3	97
10	8×10^3	8.24×10^3	103
11	16×10^3	15.52×10^3	97

showed an excellent photocurrent signal for the first time. In addition, we also regarded the L-Cys bilayers/L-Cys-hemin/G-quadruplex as a signal amplification with self-catalytic performance. It is worth mentioning that the G-quadruplex of the L-Cys bilayers/L-Cys-hemin/G-quadruplex was the product formed by the RCA process, so we could obtain a large amount of self-catalytic enzymes in a short time to achieve strong photocurrent signal. The new type of PEC sensor was used to detect CysC highly sensitively. Due to the easy separation and rough recombination of electron−hole pairs and high porosity, Ti-MOF@DM-LZU1@Au can provide a strong photocurrent. L-Cys bilayers/L-Cys-hemin achieved noticeable improvement in the PEC sensor effect by generating H_2O_2 in situ and shortening the distance between L-Cys molecules. The constructed PEC sensor realized the ultrasensitive detection of CysC, with a detection range of 10 pg/mL to 16 μg/mL and a lower limit of 8.023 pg/mL. The experimental data showed that the biosensor had good repeatability, selectivity, and stability. Moreover, this PEC sensor strategy provided a new method and idea for the highly sensitive and rapid detection of other protein molecules in clinical practice.

■ ASSOCIATED CONTENT

Supporting Information

The Supporting Information is available free of charge at https://pubs.acs.org/doi/10.1021/acsomega.4c01644.

Sequences of all DNA; XRD patterns of Ti-MOF, DM-LZU1, the core−shell Ti-MOF@DM-LZU1, and Ti-MOF@DM-LZU1@Au; FT-IR spectra of Ti-MOF, DM-LZU1, Ti-MOF@DM-LZU1, and Ti-MOF@DM-LZU1@Au; optimization of the bioassay conditions based on the PEC responses; different signal amplification strategies; specificity, repeatability, and stability characterizations of the PEC biosensor (Figures S1 to S5 and Table S1) (PDF)

■ AUTHOR INFORMATION

Corresponding Authors

Xiaolong Wang − *Emergency Department, Second Affiliated Hospital of Chongqing Medical University, Chongqing 400010, China*; Email: wang.xiaolong@cqmu.edu.cn

Yan Li − *Analytical & Testing Center, Laboratory Construction and Equipment Management Division, Southwest University, Chongqing 400715, China; Department of Clinical and Military Laboratory Medicine, College of Pharmacy and Laboratory Medicine, Army Medical University (Third Military Medical University), Chongqing 400038, China;* orcid.org/0000-0002-7254-6382; Email: yanli0345@163.com

Authors

Mengshi Xia − *Emergency Department, Second Affiliated Hospital of Chongqing Medical University, Chongqing 400010, China*

Pan Yang − *Emergency Department, Second Affiliated Hospital of Chongqing Medical University, Chongqing 400010, China*

Chuiyu Zhu − *Department of Clinical and Military Laboratory Medicine, College of Pharmacy and Laboratory Medicine, Army Medical University (Third Military Medical University), Chongqing 400038, China*

Yue Hu − *Emergency Department, Second Affiliated Hospital of Chongqing Medical University, Chongqing 400010, China*

Lichao Fang − *Department of Clinical and Military Laboratory Medicine, College of Pharmacy and Laboratory Medicine, Army Medical University (Third Military Medical University), Chongqing 400038, China*

Junsong Zheng − *Department of Clinical and Military Laboratory Medicine, College of Pharmacy and Laboratory Medicine, Army Medical University (Third Military Medical University), Chongqing 400038, China;* orcid.org/0000-0002-5248-4209

Complete contact information is available at: https://pubs.acs.org/10.1021/acsomega.4c01644

Author Contributions

‖M.X. and P.Y. contributed equally.

Notes

The authors declare no competing financial interest.

■ ACKNOWLEDGMENTS

This work was supported by the National Natural Science Foundation of China (No. 81972024) and the Natural Science Foundation Project of CQ CSTC (cstc2020jcyj-msxmX0464) and the Chongqing Graduate Research Innovation Project (CYS22350).

■ ABBREVIATIONS

AKI, acute kidney injury; AuNPs, Au nanoparticles; AA, L-ascorbic acid; BSA, bovine serum albumin; CysC, cystatin C; COF, covalent organic framework; CTAB, cetyltrimethylammonium bromide; CV, cyclic voltammetry; DMSO, dimethyl sulfoxide; EIS, electrochemical impedance spectroscopy; EDC, 1-(3-dimethylaminopropyl)-3-ethylcarbodiimide; FT-IR, Fourier transform infrared spectrometer; GFR, glomerular filtration rate; H_2O_2, hydrogen peroxide; ITO, indium tin oxides; $HAuCl_4$, gold acid chloride; LCCT, linker-to-metal-cluster charge-transfer; NHS, *N*-hydroxy succinimide; PEC, photoelectrochemical; ProA, protein A; PSA, prostate-specific antigen; RCA, rolling circle amplification; SEM, scanning electron microscope; TEM, transmission electron microscope; TCEP, tris(2-carboxyethyl) phosphine; THAM, tris(hydroxymethyl) aminomethane

■ REFERENCES

(1) Balakrishna, A.; Walco, J.; Billings, F. T. T.; Lopez, M. G. Perioperative Acute Kidney Injury: Implications, Approach. *Prevention. Adv. Anesth* **2023**, *41* (1), 205−224.

(2) Yoon, S. Y.; Kim, J. S.; Jeong, K. H.; Kim, S. K. Acute Kidney Injury: Biomarker-Guided Diagnosis and Management. *Medicina (Kaunas)* **2022**, *58* (3), 340−256.
(3) Lima, C.; Gorab, D. L.; Fernandes, C. R.; Macedo, E. Role of proenkephalin in the diagnosis of severe and subclinical acute kidney injury during the perioperative period of liver transplantation. *Pract Lab Med.* **2022**, *31*, No. e00278.
(4) Davis, J.; Rossi, G.; Cianciolo, R. E.; Ho, K. M.; Hosgood, G. L.; Miller, D. W.; Raisis, A. L. Early diagnosis of acute kidney injury subsequent to severe hypotension and fluid resuscitation in anaesthetized dogs. *Vet Anaesth Analg* **2022**, *49* (4), 344−353.
(5) Yang, D.; Zhao, L.; Kang, J.; Wen, C.; Li, Y.; Ren, Y.; Wang, H.; Zhang, S.; Yang, S.; Song, J.; Gao, D.; Li, Y. Development and validation of a predictive model for acute kidney injury in patients with moderately severe and severe acute pancreatitis. *Clin Exp Nephrol* **2022**, *26* (8), 770−787.
(6) Bíró, E.; Szegedi, I.; Kiss, C.; Oláh, A. V.; Dockrell, M.; Price, R. G.; Szabó, T. The role of urinary N-acetyl-β-D-glucosaminidase in early detection of acute kidney injury among pediatric patients with neoplastic disorders in a retrospective study. *BMC Pediatr* **2022**, *22* (1), 429.
(7) Dutta, A.; Saha, S.; Bahl, A.; Mittal, A.; Basak, T. A comprehensive review of acute cardio-renal syndrome: need for novel biomarkers. *Front. Pharmacol.* **2023**, *14*, 1152055.
(8) Abadeer, M.; Swartz, M. F.; Martin, S. D.; Groves, A. M.; Kent, A. L.; Schwartz, G. J.; Brophy, P.; Alfieris, G. M.; Cholette, J. M. Using Serum Cystatin C to Predict Acute Kidney Injury Following Infant Cardiac Surgery. *Pediatr Cardiol* **2023**, *44* (4), 855−866.
(9) Sun, H.; Gong, W.; Cong, S.; Liu, C.; Song, G.; Lu, W.; Zhao, Z. Ultrathin Two-Dimensional Metal-Organic Framework Nanosheets with Activated Ligand-Cluster Units for Enhanced SERS. *ACS Appl. Mater. Interfaces* **2022**, *14* (1), 2326−2334.
(10) Yu, S.; Xiao, Y.; Liu, Z.; Lyu, J. M.; Wang, Y. L.; Hu, Z. Y.; Li, Y.; Sun, M. H.; Chen, L. H.; Su, B. L. Ti-MOF single-crystals featuring an intracrystal macro-microporous hierarchy for catalytic oxidative desulfurization. *Chem. Commun. (Camb)* **2023**, *59* (13), 1801−1804.
(11) Hossain, A.; Meera, M. S.; Mukhanova, E. A.; Soldatov, A. V.; Henaish, A. M. A.; Ahmed, J.; Mao, Y.; Shibli, S. M. A. Influences of Partial Destruction of Ti-MOFs on Photo(electro)catalytic H(2) Evolution by Dominating Role of Charge Carrier Trapping over Surface Area. *Small* **2023**, *19* (26), No. e2300492.
(12) Ye, G.; Yang, Z.; Wan, L.; Shi, G.; Chang, Y.; Zhang, Q. Insights into the sacrificial structure-activity relationship of a Ti-based metal-organic framework in an oxidative desulfurization reaction. *Dalton Trans* **2023**, *52* (43), 15968−15973.
(13) Liu, M.; Wen, J.; Xiao, R.; Tan, R.; Qin, Y.; Li, J.; Bai, Y.; Xi, M.; Yang, W.; Fang, Q.; Hu, L.; Gu, W.; Zhu, C. Improving Interface Matching in MOF-on-MOF S-Scheme Heterojunction through pi-pi Conjugation for Boosting Photoelectric Response. *Nano Lett.* **2023**, *23* (11), 5358−5366.
(14) Sasmal, H. S.; Kumar Mahato, A.; Majumder, P.; Banerjee, R. Landscaping Covalent Organic Framework Nanomorphologies. *J. Am. Chem. Soc.* **2022**, *144* (26), 11482−11498.
(15) Qin, J.; Li, J.; Zeng, H.; Tang, J.; Tang, D. Recent advances in metal−organic framework-based photoelectrochemical and electrochemiluminescence biosensors. *Analyst* **2023**, *148* (10), 2200−2213.
(16) Dai, J.; Wilhelm, K. B.; Bischoff, A. J.; Pereira, J. H.; Dedeo, M. T.; García-Almedina, D. M.; Adams, P. D.; Groves, J. T.; Francis, M. B. A Membrane-Associated Light-Harvesting Model is Enabled by Functionalized Assemblies of Gene-Doubled TMV Proteins. *Small* **2023**, *19* (20), No. e2207805.
(17) Niu, J.; Yuan, M.; Chen, J.; Wang, L.; Qi, Y.; Bai, K.; Fan, Y.; Gao, P. L-Cysteine-Modified Transfersomes for Enhanced Epidermal Delivery of Podophyllotoxin. *Molecules* **2023**, *28* (15), 5712.
(18) Su, Y.; Hessou, E. P.; Colombo, E.; Belletti, G.; Moussadik, A.; Lucas, I. T.; Frochot, V.; Daudon, M.; Rouzière, S.; Bazin, D.; Li, K.; Quaino, P.; Tielens, F. Crystalline structures of L-cysteine and L-cystine: a combined theoretical and experimental characterization. *Amino Acids* **2022**, *54* (8), 1123−1133.
(19) Li, T. T.; Xin, D. Q.; Ke, H. F.; Chu, X. L.; Zhao, Y. J.; Yue, S. W.; Liu, D. X.; Wang, Z. L-Cysteine attenuates osteopontin-mediated neuroinflammation following hypoxia-ischemia insult in neonatal mice by inducing S-sulfhydration of Stat3. *Acta Pharmacol Sin* **2022**, *43* (7), 1658−1669.
(20) Kawakami, T.; Sasakura, E.; Miyanoiri, Y.; Hojo, H. Relative configuration of Cys-Pro ester peptides in thioester formation. *J. Pept Sci.* **2022**, *28* (8), No. e3406.
(21) Peng, J.; Huang, Q.; Zhuge, W.; Liu, Y.; Zhang, C.; Yang, W.; Xiang, G. Blue-light photoelectrochemical sensor based on nickel tetra-amined phthalocyanine-graphene oxide covalent compound for ultrasensitive detection of erythromycin. *Biosens Bioelectron* **2018**, *106*, 212−218.
(22) Yu, S.; Liu, Z.; Lyu, J. M.; Guo, C. M.; Wang, Y. L.; Hu, Z. Y.; Li, Y.; Sun, M. H.; Chen, L. H.; Su, B. L. Intraparticle ripening to create hierarchically porous Ti-MOF single crystals for deep oxidative desulfurization. *Dalton Trans* **2023**, *52* (35), 12244−12252.
(23) Fischer, A.; Zhang, P.; Ouyang, Y.; Sohn, Y. S.; Karmi, O.; Nechushtai, R.; Pikarsky, E.; Willner, I. DNA-Tetrahedra Corona-Modified Hydrogel Microcapsules: "Smart" ATP- or microRNA-Responsive Drug Carriers. *Small* **2022**, *18* (52), No. e2204108.
(24) Rojas, S.; García-González, J.; Salcedo-Abraira, P.; Rincón, I.; Castells-Gil, J.; Padial, N. M.; Marti-Gastaldo, C.; Horcajada, P. Ti-based robust MOFs in the combined photocatalytic degradation of emerging organic contaminants. *Sci. Rep* **2022**, *12* (1), 14513.
(25) Yoshida, S.; Tomizaki, K. Y.; Usui, K. Shape control of Au nanostructures using peptides for biotechnological applications. *Chem. Commun. (Camb)* **2023**, *59* (89), 13239−13244.
(26) Zhu, C.; Tian, X.; Li, Q.; Dai, Z.; Wang, L.; Liu, H.; Li, C.; Zahid, K. R.; Wu, C.; Huang, H.; Fang, L.; Huang, Q.; Liu, F.; Deng, J.; Li, Y.; Zeng, T.; Zheng, J. Ultrasensitive photoelectrochemical biosensor for DNA 5-methylcytosine analysis based on co-sensitization strategy combined with bridged DNA nanoprobe. *Talanta* **2023**, *254*, No. 124140.
(27) He, X.; Ding, Y.; Huang, Z.; Liu, M.; Chi, M.; Wu, Z.; Segre, C. U.; Song, C.; Wang, X.; Guo, X. Engineering a Self-Grown TiO(2) /Ti-MOF Heterojunction with Selectively Anchored High-Density Pt Single-Atomic Cocatalysts for Efficient Visible-Light-Driven Hydrogen Evolution. *Angew. Chem., Int. Ed. Engl.* **2023**, *62* (25), No. e202217439.
(28) Sowersby, D. S.; Lewis, L. K. SURE gel electrophoresis: A method for improved detection and purification of dilute nucleic acid samples. *Anal. Biochem.* **2024**, *684*, No. 115373.
(29) Svitková, V.; Konderíková, K.; Nemčeková, K. Photoelectrochemical aptasensors for detection of viruses. *Monatsh. Chem.* **2022**, *153* (11), 963−970.
(30) Mi, L.; Wang, P.; Yan, J.; Qian, J.; Lu, J.; Yu, J.; Wang, Y.; Liu, H.; Zhu, M.; Wan, Y.; Liu, S. A novel photoelectrochemical immunosensor by integration of nanobody and TiO_2 nanotubes for sensitive detection of serum cystatin C. *Anal. Chim. Acta* **2016**, *902*, 107−114.
(31) Ferreira, P. A.; Araujo, M. C.; Prado, C. M.; De Lima, R. A.; Rodríguez, B. A.; Dutra, R. F. An ultrasensitive Cystatin C renal failure immunosensor based on a PPy/CNT electrochemical capacitor grafted on interdigitated electrode. *Colloids Surf., B* **2020**, *189*, No. 110834.
(32) Bargnoux, A. S.; Azoury, V.; Badiou, S.; Klouche, K.; Plawecki, M.; Kuster, N.; Cristol, J. P. Analytical performances of PENIA and PETIA urinary cystatin C determination allow tubular injury investigation. *Ann. Clin Biochem* **2019**, *56* (2), 228−231.
(33) Trindade, E. K. G.; Silva, B. V. M.; Dutra, R. F. A probeless and label-free electrochemical immunosensor for cystatin C detection based on ferrocene functionalized-graphene platform. *Biosens Bioelectron* **2019**, *138*, 111311.

https://doi.org/10.1021/acsomega.4c01644
ACS Omega 2024, 9, 28228−28236